

# *Tianwen-1 and MAVEN observations of the response of Mars to an interplanetary coronal mass ejection*

Article

Published Version

Creative Commons: Attribution 4.0 (CC-BY)

Open Access

Yu, B., Chi, Y., Owens, M. ORCID: <https://orcid.org/0000-0003-2061-2453>, Scott, C. J. ORCID: <https://orcid.org/0000-0001-6411-5649>, Shen, C., Xue, X., Barnard, L. ORCID: <https://orcid.org/0000-0001-9876-4612>, Zhang, T., Heyner, D., Auster, H.-U., Richter, I., Guo, J., Sánchez-Cano, B., Pan, Z., Zou, Z., Su, Z., Wu, Z., Wang, G., Xiao, S., Liu, K., Hao, X., Li, Y., Chen, M., Dou, X. and Lockwood, M. ORCID: <https://orcid.org/0000-0002-7397-2172> (2023) Tianwen-1 and MAVEN observations of the response of Mars to an interplanetary coronal mass ejection. The Astrophysical Journal, 953 (1). 105. ISSN 0004-637X doi: 10.3847/1538-4357/acdcf8 Available at <https://centaur.reading.ac.uk/112197/>

It is advisable to refer to the publisher's version if you intend to cite from the work. See [Guidance on citing](#).

To link to this article DOI: <http://dx.doi.org/10.3847/1538-4357/acdcf8>

Publisher: American Astronomical Society

All outputs in CentAUR are protected by Intellectual Property Rights law, including copyright law. Copyright and IPR is retained by the creators or other copyright holders. Terms and conditions for use of this material are defined in the [End User Agreement](#).

[www.reading.ac.uk/centaur](http://www.reading.ac.uk/centaur)

## **CentAUR**

Central Archive at the University of Reading

Reading's research outputs online



# Tianwen-1 and MAVEN Observations of the Response of Mars to an Interplanetary Coronal Mass Ejection

Bingkun Yu<sup>1</sup>, Yutian Chi<sup>1</sup>, Mathew Owens<sup>2</sup>, Christopher J. Scott<sup>2</sup>, Chenglong Shen<sup>3,4,5</sup>, Xianghui Xue<sup>3,5,6,7</sup>, Luke Barnard<sup>2</sup>, Tielong Zhang<sup>5,8</sup>, Daniel Heyner<sup>9</sup>, Hans-Ulrich Auster<sup>9</sup>, Ingo Richter<sup>9</sup>, Jingnan Guo<sup>4,5</sup>, Beatriz Sánchez-Cano<sup>10</sup>, Zonghao Pan<sup>4,5</sup>, Zhuxuan Zou<sup>3</sup>, Zhenpeng Su<sup>4,5</sup>, Zhiyong Wu<sup>3</sup>, Guoqiang Wang<sup>11</sup>, Sudong Xiao<sup>11</sup>, Kai Liu<sup>4,5</sup>, Xinjun Hao<sup>4,5</sup>, Yiren Li<sup>4,5</sup>, Manming Chen<sup>4,5</sup>, Xiankang Dou<sup>3,7</sup>, and Mike Lockwood<sup>2</sup>

<sup>1</sup>Institute of Deep Space Sciences, Deep Space Exploration Laboratory, Hefei, People's Republic of China

<sup>2</sup>Department of Meteorology, University of Reading, Berkshire, UK

<sup>3</sup>CAS Key Laboratory of Geospace Environment, Department of Geophysics and Planetary Sciences, University of Science and Technology of China, Hefei, People's Republic of China; [xuexh@ustc.edu.cn](mailto:xuexh@ustc.edu.cn)

<sup>4</sup>Deep Space Exploration Laboratory/School of Earth and Space Sciences, University of Science and Technology of China, Hefei, People's Republic of China

<sup>5</sup>CAS Center for Excellence in Comparative Planetology, University of Science and Technology of China, Hefei, People's Republic of China

<sup>6</sup>Anhui Mengcheng Geophysics National Observation and Research Station, University of Science and Technology of China, Mengcheng, Anhui, People's Republic of China

<sup>7</sup>Hefei National Laboratory for the Physical Sciences at the Microscale, University of Science and Technology of China, Hefei, People's Republic of China

<sup>8</sup>Space Research Institute, Austrian Academy of Sciences, Graz, Austria

<sup>9</sup>Institut für Geophysik und extraterrestrische Physik, Technische Universität Braunschweig, Braunschweig, Germany

<sup>10</sup>School of Physics and Astronomy, University of Leicester, Leicester, UK

<sup>11</sup>Institute of Space Science and Applied Technology, Harbin Institute of Technology, Shenzhen, People's Republic of China

Received 2023 April 12; revised 2023 June 3; accepted 2023 June 7; published 2023 August 8

## Abstract

Interplanetary coronal mass ejections (ICMEs) are solar transients that have significant effects on the upper atmosphere and ionosphere of Mars. The simultaneous spacecraft observations from Tianwen-1/MOMAG in solar wind and multiple instruments on board the Mars Atmosphere and Volatile Evolution (MAVEN) in the Martian upper atmosphere are used to study the response of Mars to an ICME. The ICME was observed at Mars by Tianwen-1 and MAVEN at 00:00 UT on 2021 December 10, which was earlier observed by BepiColombo upstream of Mars at 22:32 UT on 2021 December 6. During 2021 December 6–15, MAVEN measured the nightside ionosphere and Tianwen-1 measured the dayside ionosphere while both were inside the Martian bow shock. The rapid drop in densities of ionospheric ions and electrons, which is typically identified as the end of the ionosphere at altitudes between 300–800 km, is known as the ionopause. The altitude of the Martian ionopause location was lowered by the high dynamic pressure of the solar wind during the ICME passage. The depletion of the plasma density in the topside Martian ionosphere on the nightside reveals the presence of substantial ion and electron escape to space through the interaction between the ICME and Mars. The column abundance of plasma dramatically decreased, with 34%  $e^-$ , 61%  $O_2^+$ , and 73%  $O^+$  reduced. This study highlights the significant impact of the space weather associated with the intense magnetic field and high dynamic pressure of the ICME on Mars's atmosphere, which is particularly important for future human exploration missions to Mars.

*Unified Astronomy Thesaurus concepts:* Solar coronal mass ejections (310); Solar system terrestrial planets (797)

## 1. Introduction

Coronal mass ejections (CMEs) are large-scale episodic eruptions of coronal mass and magnetic flux ejected out from the lower solar corona into the heliosphere (Yashiro et al. 2004; Davis et al. 2009; Lee et al. 2013). Interplanetary coronal mass ejections (ICMEs), the interplanetary counterparts of CMEs, propagate through interplanetary space and drive severe space weather in planetary environments (Richardson & Cane 2012; Chi et al. 2016, 2021; Zhang et al. 2021b). ICMEs with large-scale expulsions of plasma (Zhang et al. 2021b), highly structured magnetic fields (Lepping & Wu 2007; Wu et al. 2013; Lockwood et al. 2016), and preceded by a fast-forward shock (Wang et al. 2021a; Xu et al. 2022) can significantly distort the Earth's magnetosphere (Lockwood et al. 2016, 2019) and cause intense geomagnetic storms (Xue et al. 2005;

Zhang et al. 2007; Shen et al. 2017; Chi et al. 2021; Mishra et al. 2021; Owens et al. 2021). Geomagnetic storms cause a series of disturbances in the Earth's thermosphere (Lockwood et al. 2016), ionosphere (Younas et al. 2020; Yu et al. 2021), magnetosphere (Lockwood et al. 2020), and thermosphere (Wang et al. 2021b). The arrival of ICMEs and the potential effects of space weather on the performance of ground-based technological systems and the Global Navigation Satellite System (GNSS) positioning might endanger human health or even life (Knipp et al. 2016). Approximately 87% intense geomagnetic storms ( $Dst \leq -100$  nT) were caused by ICMEs (Shen et al. 2017). The intensity of geomagnetic storms mainly depends on the magnetic-field intensity and the speed within the ejecta of the ICME (Chi et al. 2016).

At Earth, the magnetosphere shields the atmosphere from the solar wind. Since Mars lacks a global intrinsic magnetic field, the solar wind can more easily affect the atmosphere. Planetary plasma escape is an efficient loss process subject to direct or indirect solar wind forcing (Lundin 2011) and is an important process in the evolution of the Martian atmosphere. Although



Original content from this work may be used under the terms of the [Creative Commons Attribution 4.0 licence](https://creativecommons.org/licenses/by/4.0/). Any further distribution of this work must maintain attribution to the author(s) and the title of the work, journal citation and DOI.

the intrinsic magnetic field from the Martian magnetic anomalies provides some magnetic shielding, it is insufficient to prevent solar wind energy and momentum from directly accessing the Martian upper ionosphere (e.g., Lundin et al. 2004; Dubinin et al. 2006). This leads to a scavenging of ionospheric heavy ions ( $O^+$ ,  $O_2^+$ , and  $CO_2^+$ ) from the dayside toward the nightside/tail (Lundin 2011). Mars's atmospheric ion species escape the planet and flow into space, where they are blown away by solar wind (Carlsson et al. 2006; Benna et al. 2015). Electron depletions are observed at altitudes between 110–900 km in the Martian environment, particularly on the nightside (Hall et al. 2016). It is now well-accepted that ICMEs are the solar transients that have the greatest effect on the space environment and cause the most adverse space weather effect (Zhang et al. 2021b). ICME events significantly affect the structure of the upper atmosphere and ionosphere of Mars, and influence the loss of ions to space (Jakosky et al. 2015; Sánchez-Cano et al. 2017; Kajdič et al. 2021). Therefore, ICMEs play an important role in driving plasma escape and the evolution of the Martian atmosphere. However, the limitations of spacecraft observations make it difficult to advance our scientific understanding of ICME-driven planetary plasma escape from the Martian ionosphere.

The ICME interactions with Mars have previously been studied from measurements obtained by several Mars missions, including the Mars Atmosphere and Volatile Evolution (MAVEN), Mars Express (MEX), Mars Science Laboratory (MSL), Mars Odyssey (MO), and Trace Gas Orbiter (TGO). One special GRL issue focused on the space weather impacts of the 2017 September 10 solar eruptive event on the Martian upper atmosphere system. A fast CME erupted on 2017 September 10 and arrived at Mars on 2017 September 13. With the enhanced dynamic pressure from the ICME, the draped interplanetary magnetic field (IMF) reached down to 200 km altitude into the Martian atmosphere. In general, the average ion escape flux is enhanced by a factor of  $\sim 2$  during the ICME (Lee et al. 2018). The ionospheric magnetic field of Mars was globally amplified in response to the high dynamic pressure of solar wind during the ICME passage, with a rise in nightside peak electron density at altitudes of 120 km (Harada et al. 2018). The results of magnetohydrodynamic model suggest a deeper IMF penetration and more open field lines in the Martian magnetic topology in response to the ICME (Xu et al. 2018). During the ICME, the solar wind conditions were more disrupted, which caused a greater variation in the plasma boundary positions and an intensification of the ion loss rate (Ma et al. 2018).

The Tianwen-1 spacecraft is China's first Mars exploration mission. It was launched on 2020 July 23 from Wenchang Space Launch Center on Hainan Island and entered into a Mars orbit on 2021 February 10 (Wan et al. 2020). Tianwen-1 aims to carry out a comprehensive study of Mars by orbiting, landing, and roving in one mission. It makes thorough global and local surveys using both the orbiter and the rover. The Tianwen-1 payload comprises 13 instruments; seven instruments on board the orbiter and six instruments installed on the Zhurong rover (Zou et al. 2021). The seven scientific instruments on board the orbiter include the Moderate Resolution Imaging Camera (MoRIC; Yu et al. 2020), the High-Resolution Imaging Camera (HiRIC; Meng et al. 2021), the Mars Orbiter Scientific Investigation Radar (MOSIR; Fan et al. 2021), the Mars Mineralogical Spectrometer (MMS; He et al. 2021), the Mars Orbiter Magnetometer (MOMAG; Liu

et al. 2020), the Mars Ion and Neutral Particle Analyzer (MINPA; Kong et al. 2020), and the Mars Energetic Particles Analyzer (MEPA; Tang et al. 2020). One of Tianwen-1's scientific objectives is to study the Martian ionosphere and survey the interplanetary environment.

The recently released Tianwen-1/MOMAG data and MAVEN data are used to study the response of the Martian ionosphere to a strong ICME between 2021 December 8 and December 13. Chi et al. (2023a) identified two ICME and three SIR events detected between 2021 November 16, and 2021 December 31, using the first publicly available Tianwen-1/MOMAG data that was gathered in the first one and a half months, combined with MAVEN data. The GCS cone model and Huxt solar wind model were used to show the interplanetary evolution of the ICMEs and to forecast whether the CME will hit the spacecraft by comparison of the arrival time and velocity of solar wind with the in situ data at Mars. However, the effects of these ICME events on the space environment at Mars were not analyzed.

The main goal of this work is to understand the real-time behavior of the Martian ionosphere during the impact of an ICME with simultaneous spacecraft observations from Tianwen-1/MOMAG and multiple instruments on board MAVEN. This is the first time that this type of investigation can be done because of the multi-spacecraft opportunity scenario. Figure 1 shows a sketch illustrating the Tianwen-1, MAVEN, and BepiColombo measurements of the response of Martian upper atmosphere and ionosphere to an ICME. Section 2 describes the data used in the study. In Section 3, the in situ observations of the ICME arriving at Mars and its subsequent impacts on Mars are presented using MAVEN and Tianwen-1 measurements. Section 4 summarizes the conclusions of this paper.

## 2. Data Description

Tianwen-1 was launched on 2020 July 23 and entered Mars orbit on 2021 February 10. The Tianwen-1 orbiter is in a highly inclined elliptical orbit at an inclination of  $86^\circ.9$ . The orbit of Tianwen-1 is at a periapsis altitude of  $\sim 265$  km and a periapsis altitude of  $\sim 12,000$  km with a period of 7.8 hr. The MOMAG instrument on board Tianwen-1 has routinely measured the magnetic field from solar wind to the magnetic pileup region surrounding Mars since 2021 November 13 (Wang et al. 2023). In 2021 December, the orbital periapsis was on the dayside above the northern pole of Mars and the apoapsis was far from the southern pole on the nightside. Tianwen-1/MOMAG typically measures the ambient magnetic field with a high sampling frequency of 32 Hz. In this study, the magnetic field data were obtained at a resolution of 1 second derived from the full-resolution source data. The MOMAG level 2 archive data have been released at the Planet Exploration Program Scientific Data Release System. The MOMAG data used in this study are publicly available on the official website of the MOMAG team at the University of Science and Technology of China (USTC, [http://space.ustc.edu.cn/dreams/tw1\\_momag/](http://space.ustc.edu.cn/dreams/tw1_momag/)). Further details on the calibration procedures and in-flight performance of Tianwen-1/MOMAG, including individual comparisons with simultaneous MAVEN/MAG measurements between 2021 November 13 and December 31, can be found in the references (Wang et al. 2023; Zou et al. 2023).

MAVEN was launched on 2013 November 18 and began its science operations at Mars in 2014 November (Halekas et al.



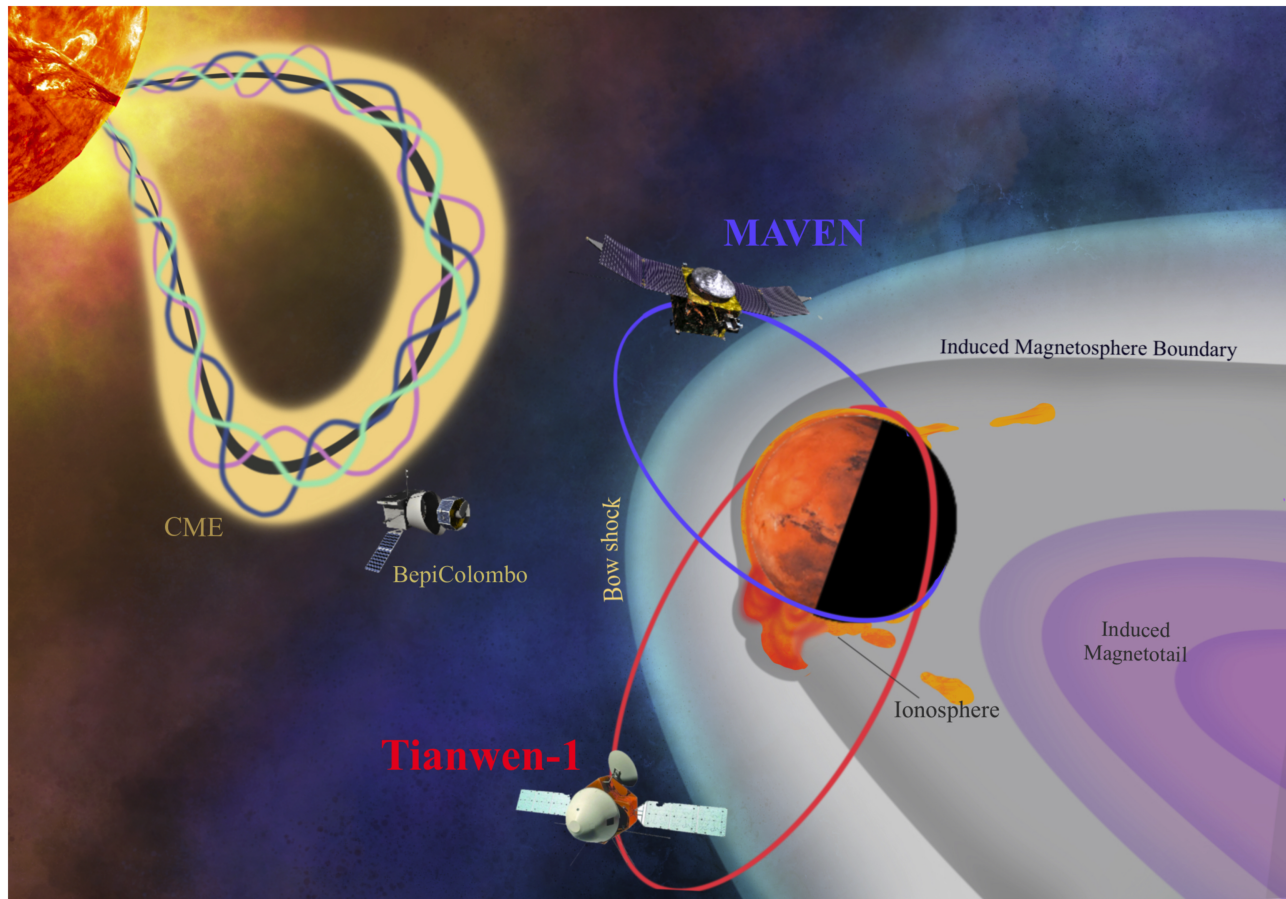


**Figure 1.** Illustration of Tianwen-1, MAVEN, and BepiColombo in situ measurements of the response of Martian upper atmosphere and ionosphere to an interplanetary coronal mass.

2017; Lee et al. 2017). One of its prime science goals is to understand the atmospheric escape of Mars. The MAVEN spacecraft is in an elliptical orbit, with a periaapsis altitude of  $\sim 150$  km, apoapsis altitude of  $\sim 6200$  km, and period of 4.5 hr. The ambient vector magnetic field is measured by the magnetometer (MAG) instrument on board MAVEN (Connerney et al. 2015). The density, temperature, bulk flow velocities, and dynamic pressure around Mars are measured by the solar wind ion analyzer (SWIA) instrument (Halekas et al. 2015). The density and composition of neutral atoms and ions in the upper atmosphere of Mars are measured by the Neutral Gas and Ion Mass Spectrometer (NGIMS) instrument (Mahaffy et al. 2015). The Langmuir Probe and Waves (LPW) instrument (Andersson et al. 2015) measures the electron density and temperature in the ionosphere of Mars.

In addition, we use BepiColombo observations upstream of Mars. BepiColombo was launched in 2018 and will enter Mercury orbit in late 2025 after a 7.2 yr voyage. Although the primary objective of the magnetometer instrument (MPO-MAG; Glassmeier et al. 2010; Heyner et al. 2021) on the Mercury Planetary Orbiter of the BepiColombo mission is to characterize Mercury’s planetary magnetic field (Benkhoff et al. 2021), it can provide accurate in situ measurements of the IMF while traveling to Mercury. The 1 s high-resolution BepiColombo/MPO-MAG data were used to identify ICMEs at 0.67 au upstream Mars between 2021 December 6 and December 8.

### 3. Observational Results

#### 3.1. The Ejecta of an ICME Arrived at Mars at 00:00 UT on 2021 December 10

Chi et al. (2023b) presented a detailed study of the evolution of two ICME events, which were detected by BepiColombo in the solar wind, and by Tianwen-1 and MAVEN at Mars in 2021 December. They studied the evolution of the ICME from the Sun to Mars, but they did not investigate the planetary effects of these space weather events. Therefore, this work focuses on the response of the Martian ionosphere to the ICMEs. One strong ICME event is of interest in this study. The ICME has a high-speed solar wind over  $500 \text{ km s}^{-1}$ , which was observed at Mars by Tianwen-1 and MAVEN from 2021 December 8 to December 13.

Figure 2(a) shows the relative position of Mars, Earth, BepiColombo, and the STEREO-A spacecraft with the ambient solar wind conditions in the ecliptic plane at 18:25 UT on 2021 December 6 estimated by the Heliospheric Upwind eXtrapolation time (HUXt) model (Owens et al. 2020; Barnard & Owens 2022). The BepiColombo spacecraft was almost aligned with Mars in the longitude of the HEEQ coordinate when the CME erupted, which can be used as the upstream solar wind monitor of Mars.

Figure 2(b) shows the orbits of Tianwen-1 (red line) and MAVEN (blue line) in a cylindrical coordinate system for the time interval from 00:00 UT on 2021 December 8 to 00:00 UT on 2021 December 13, color-coded by distance from the Mars

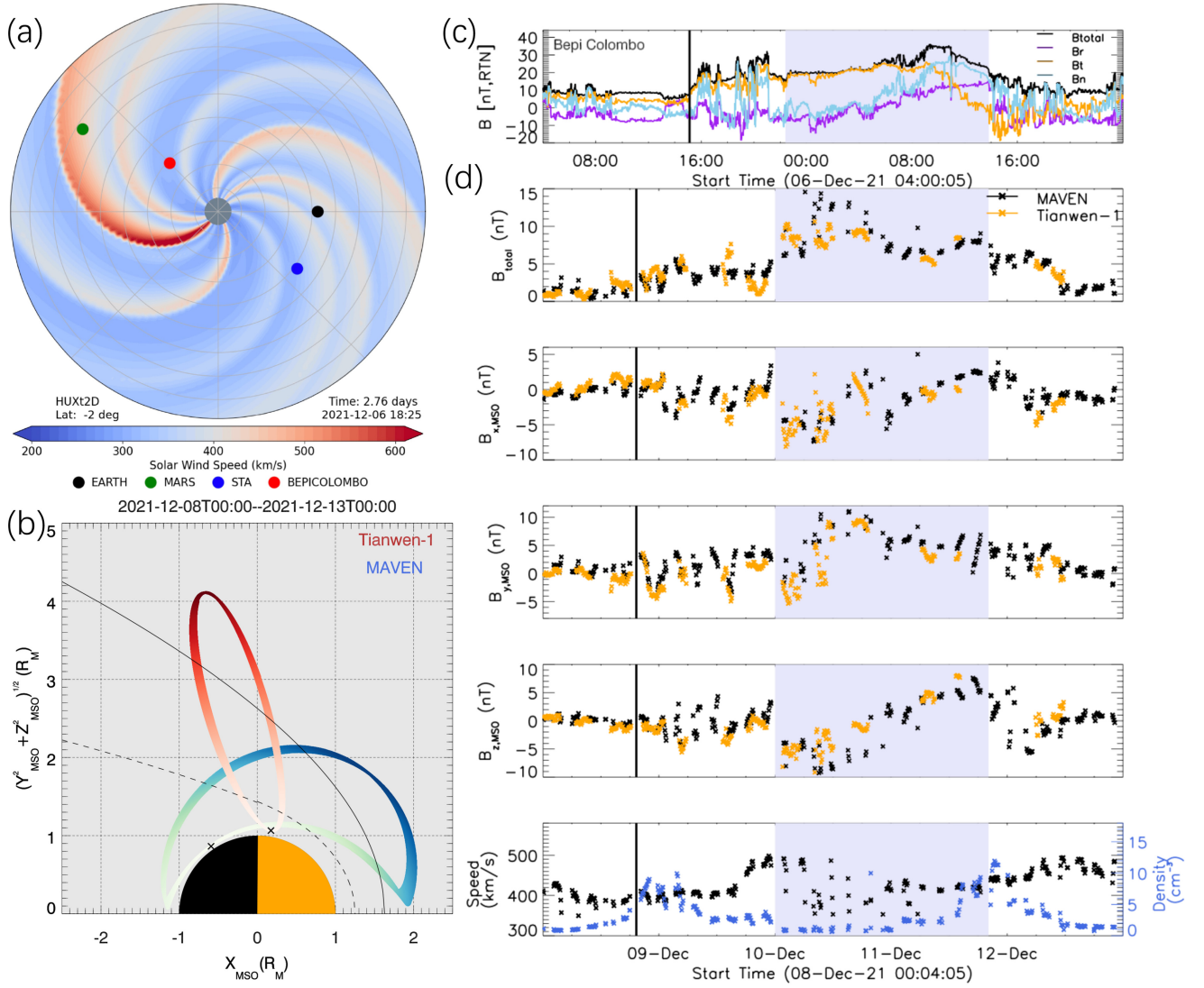


**Figure 2.** The spacecraft and planet positions on the solar equatorial plane, the orbits of Tianwen-1 and MAVEN, and the in situ solar wind observations. (a) The solar wind speed as simulated by the HUXt model with the positions of Mars and the BepiColombo spacecraft in the heliocentric Earth equatorial (HEEQ) coordinate on 2021 December 6, at 18:25 UT. (b) Trajectories of Tianwen-1 (red line) and MAVEN (blue line) in a cylindrical coordinate system for the time interval from 00:00 UT on 2021 December 8 to 00:00 UT on 2021 December 13, color-coded by distance from the Mars surface. The outer black line denotes the average location of the bow shock and the interior dashed-black line denotes the average location of the magnetic pileup boundary. (c) Magnetic observations by the BepiColombo magnetometer, showing total field strength ( $B_{total}$ ) and components ( $B_r$ ,  $B_t$ , and  $B_n$ ) in the Radial-Tangential-Normal coordinate. (d) The magnetic field, solar wind velocity, density by MAVEN, and the magnetic field by Tianwen-1. The black-vertical line represents the arrival time of the possible shock observed from the enhanced plasma density in solar wind. The purple-shaded region represents the interval of the ICME.

surface. As shown in panel (b), MAVEN’s periapsis is on the nightside and Tianwen-1’s apoapsis is on the dayside. The “x” symbols mark the MAVEN and Tianwen-1 periapsis locations. The MAVEN and Tianwen-1 periapsis solar zenith angles change slowly and systematically during successive orbits. The solar zenith angle of MAVEN periapsis is  $\sim 124^\circ$  with a periapsis altitude of  $\sim 182$  km. The solar zenith angle of Tianwen-1 periapsis is  $\sim 81^\circ$  with a periapsis altitude of  $\sim 268$  km. During 2021 November and December, Tianwen-1 apoapsis was far above the southern pole of Mars in the solar wind, spending about 50%–75% of its duration out of the magnetosheath (Wang et al. 2023). Thus, Tianwen-1/MOMAG primarily measured the IMF of the upstream solar wind of Mars. The LPW/NGIMS/MAG instruments on board MAVEN detected the response of the Martian atmosphere on the nightside.

The ICME was first observed at 0.67 au upstream of Mars by BepiColombo spacecraft. Figure 2(c) shows the magnetic-field observations from the BepiColombo/MPO-MAG in the Radial-Tangential-Normal coordinate. A forward shock was observed on December 6 at 15:07 UT, which was driven by the following ICME. The black-vertical line represents the arrival time of the shock. The purple-shaded region indicates the interval of an ICME ejecta with an enhanced and smooth changing magnetic field.

Both Tianwen-1 and MAVEN have detected the ICME at Mars. Figure 2(d) shows the in situ observations at Mars from Tianwen-1/MOMAG, MAVEN/MAG, and MAVEN/SWIA instruments. A possible forward ICME-driven shock was observed from the enhanced plasma density in solar wind at Mars on December 8 at 19:20 UT. The ejecta of the ICME arrived on December 10 at 00:00 UT and lasted for approximately 1.6 days.



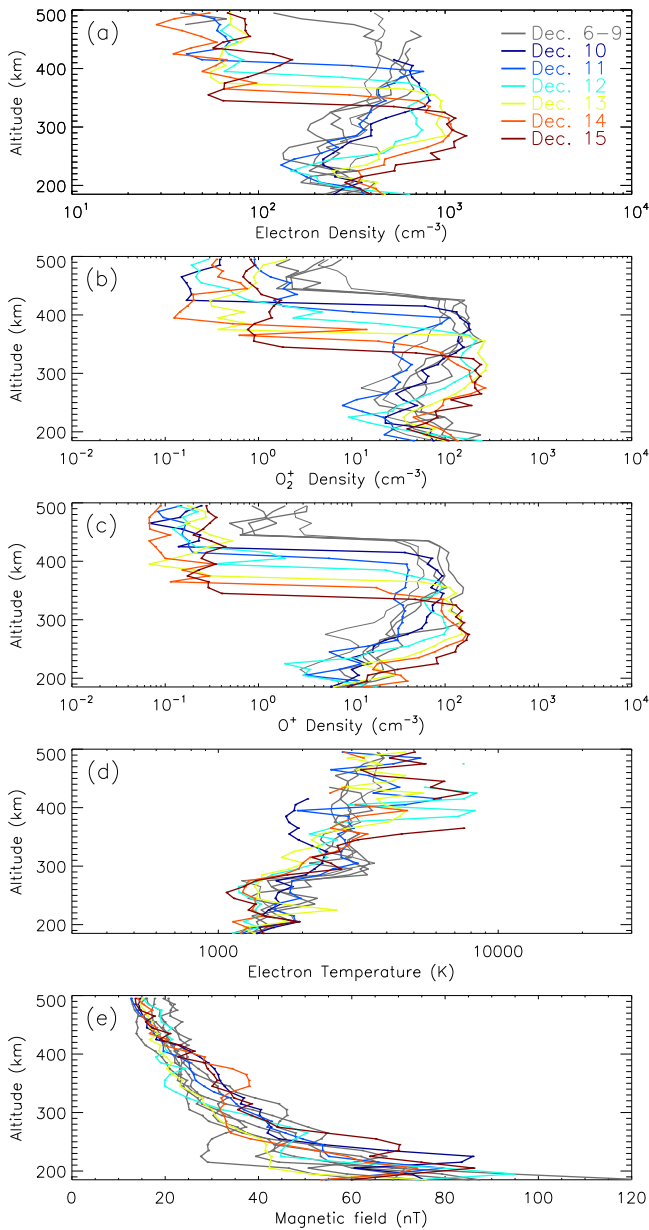


**Figure 3.** In situ observations from MAVEN at altitudes of 185–500 km on the nightside of Mars ( $X_{\text{MSO}} < 0$ ) during 2021 December 6–15. From top to bottom: (a) MAVEN/LPW electron density, (b) MAVEN/NGIMS  $\text{O}_2^+$  density, (c) MAVEN/NGIMS  $\text{O}^+$  density, (d) MAVEN/LPW electron temperature, and (e) MAVEN/MAG magnetic field in the Martian nightside ionosphere. MAVEN = Mars Atmosphere and Volatile Evolution; LPW = Langmuir Probe and Waves; NGIMS = Neutral Gas and Ion Mass Spectrometer; and MAG = Magnetometer.

### 3.2. The Response of the Martian Ionosphere to the ICME

The solar wind and Martian atmosphere have been continuously monitored by MAVEN since 2014 (Halekas et al. 2017; Lee et al. 2017). Figure 3 shows the in situ Martian observations from MAVEN LPW, NGIMS, and MAG instruments at altitudes between 185–500 km on the nightside of Mars ( $X_{\text{MSO}} < 0$ ) during 2021 December 6–15. The ionosphere was much more disturbed after December 15, due to a subsequent Stream Interaction Region (SIR) that arrived at Mars on 2021 December 16 at 06:00 UT (Chi et al. 2023a), after which the disturbances of the Martian ionosphere with the influence of the ICME are difficult to distinguish from the

influence of the SIR event. To compare the response of the ionosphere to the ICME during 2021 December 10–15, the profiles from December 6–9 were used as the background. Please note that the MAVEN profiles are not vertical. Therefore, we only utilized the nighttime ( $X_{\text{MSO}} < 0$ ,  $\text{SZA} > 90^\circ$ ) measurements of MAVEN between 185–500 km from consecutive orbits during 2021 December 6–15. The variation of solar zenith angle for these orbits at the same altitude is not very significant, making it possible to compare the MAVEN measurements along slanted orbit segments. The density profiles of the nightside ionosphere may vary from each orbit. To investigate the variations in the Martian nighttime ionosphere and its response to the ICME, a daily mean profile was calculated by taking the mean of multiple orbits.

Figure 3(a) shows the electron density from the MAVEN/LPW instrument. The gray lines reveal the typical background ionospheric profiles during December 6–9 before the arrival of ICME. The atmosphere of Mars became remarkably variable after the arrival of the ICME ejecta on 2021 December 10. The ionospheric profiles during 2021 December 10–15 are plotted in time using blue to red colors. There was no ionopause before December 10. A sudden drop in the electron density of the topside ionosphere was observed on December 10 from  $500\text{--}700\text{ cm}^{-2}$  to less than  $100\text{ cm}^{-2}$ . This signature is usually the formation of an ionopause, i.e., the uppermost side of the ionosphere. According to the daily electron density profiles, the height of the ionopause gradually decreased to 330–340 km on December 15, with an increase in electron density in the lowest region of the ionosphere below 200 km altitudes. The peak of electron density reached more than  $10^3\text{ cm}^{-2}$  at an altitude of approximately 285 km altitude on December 15.

Another criterion of the ionopause used by Vogt et al. (2015) is that the ion density decreases significantly by at least a factor of 10 over an altitude range of 30 km. Figures 3(b) and (c) show the densities of the primary  $\text{O}_2^+$  and  $\text{O}^+$  ions in the Martian nightside ionosphere from the MAVEN NGIMS instrument. According to the ion density profiles, the ionopause had already formed at an altitude of approximately 440 km altitude during December 6–9. Then, the ionopause gradually descended after the ICME arrived at Mars on December 10, and was eventually lowered to 345 km on December 15. Figure 3(d) shows the electron temperature from the MAVEN LPW instrument. The processes of plasma transport dominate the diffusion region of the Martian ionosphere above  $\sim 200$  km altitude (Sánchez-Cano et al. 2020). An increase in temperature with increasing altitude was found. The variability in electron temperature is rather small from 200–350 km altitude, where it typically increases to 2000–3000 K. The electron temperature becomes variable above 350 km. In comparison to those before the arrival of the ICME during December 6–9, the electron temperature above 350 km became visibly perturbed during December 10–15. Figure 3(e) shows the magnetic field from the MAVEN MAG instrument. The magnetic field above 350 km was nearly constant before and after the ICME. The magnetic field is larger than 30 nT at low altitudes below  $\sim 350$  km. Though the daily variation of ionosphere was calculated to minimize the effects of crustal field contributions, the ionosphere below 350 km altitude could be influenced by regions over magnetic crustal anomalies with strong magnetic fields ( $> 30$  nT).

The ICME influenced the topside ionosphere of Mars. The ICME was detected near Mars at 00:00 UT on 2021 December

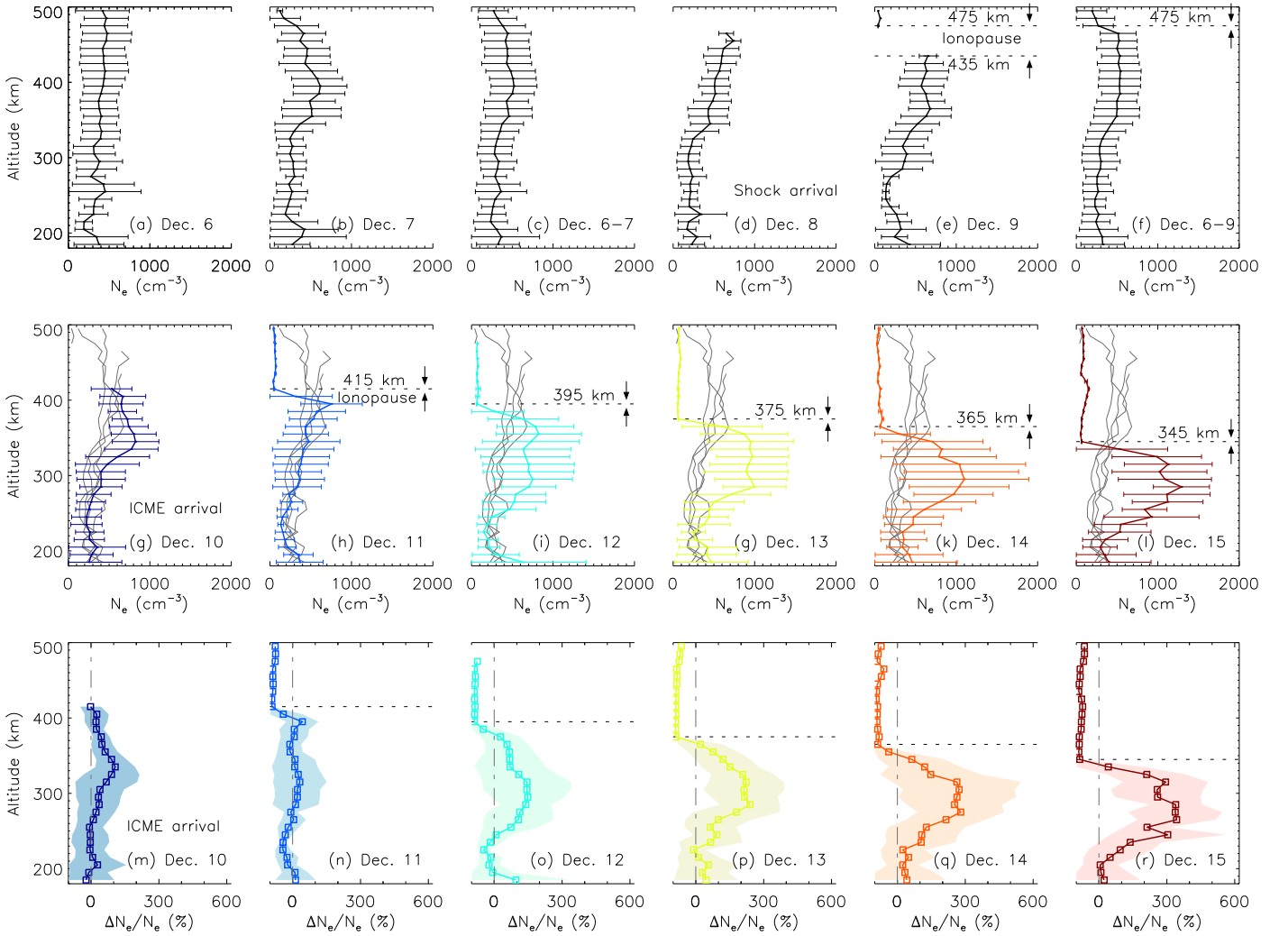


**Figure 4.** Daily altitude profiles of electron density in the Martian nightside ionosphere using MAVEN. The top six panels show the background ionospheric profiles of electron density before the ejecta of the ICME arrived at Mars. The black line represents the daily mean electron density, with the error bar representing the standard deviation in this mean. The middle six panels show the ionospheric profiles of electron density during and after the interval of the ICME by comparison with the background ionospheric profiles. The bottom six panels show the relative changes in the electron density during and after the ICME interval,  $\Delta N_e/N_e$  (%), with the shaded area representing the standard deviation.

10, and then the ionopause occurred at 330–340 km from observations of electron density in the nighttime ionosphere. With the arrival of the ICME between December 10–15, it was observed that the height of the ionopause decreased until it reached 345 km and that the electron temperature near the ionopause increased to over 8000 K. The ionopause indicates the interface between the solar wind and the ionospheric plasma. Since the ionopause divides the upper atmosphere of Mars into two distinct regimes—a plasma diffusion region below it and a region of forced convection stripping by solar wind above it where wave heating and energy transport dominate—the vertical structure of the nighttime ionosphere was changed (Nagy & Schunk 2009).

Figure 4 shows the daily altitude profiles of MAVEN/LPW electron density in the Martian nightside ionosphere. The top panels show the background electron density during December 6–9. The  $N_e$  value remained less than  $500 \text{ cm}^{-2}$  until a fast-forward shock of the ICME arrived at Mars on December 8 (Figure 4(d)), shown as a vertical line in Figure 2 detected by Tianwen-1 and MAVEN on December 8 at 19:20 UT. The ionopause cannot be identified as a result of a data gap in

electron density at a higher altitude. The electron density was depleted above 475 km on December 9. The height of the ionopause is estimated to be in the range of 435–475 km.

The middle six panels show the daily profiles of electron density in response to the ICME from December 10–15 compared with the background electron density from December 6–9. The electron density rapidly fell to depletion at a greater altitude, and the height of the ionopause showed a marked decrease. The height of the ionopause represents the lower side of the depleted electron density. In Figure 4(g), the peak of electron density was  $800 \text{ cm}^{-2}$  at 345 km, while no measurements of electron density were obtained above 415 km on December 10. Figure 4(h) shows that the topside electron density at altitudes of 415–500 km was greatly depleted, and the height of the ionopause dramatically decreased to 415 km on December 11. During December 12–15, the ionopause gradually descended, and the electron density at lower altitudes between 250–320 km was enhanced. Finally, the height of the ionopause reached 345 km on December 15. The solar energetic particles associated with the ICME could be the origin of the ionization at low altitude. The high-energy

electrons ionized the Martian atmosphere, forming a dense low ionospheric layer of ions and electrons on the Martian nightside (Sánchez-Cano et al. 2019; Krishnaprasad et al. 2021; Lester et al. 2022).

The lower six panels show the relative changes in the electron density ( $\Delta N_e/N_e$  (%)) during and after the ICME interval. The topside electron density was completely depleted. The electron depletions extended from altitudes of above 415 km on December 11 to altitudes of above 345 km on December 15. The peak of the electron density at altitudes of 260–290 km was increased by more than 300%. According to the measurements of the Martian nightside ionosphere, the plasma in the Martian nightside ionosphere was depleted, which caused the ionopause to descend gradually in response to the ICME.

For this strong ICME, the solar wind dynamic pressure and foreshock pressure of the ICME should be expected to be high, and thus the solar wind are able to penetrate downward. The decrease in the height of ionopause with solar wind compression could potentially be related to pressure changes with their own accompanying magnetic pressure. Figure 5 shows the variations in the dynamic pressure of the upstream solar wind and the ionospheric pressures with perturbations in the Martian upper atmosphere. The magnetic-field measurements from MAVEN/MAG and Tianwen-1/MOMAG, the solar wind measurements from MAVEN/SWIA, and the ionospheric plasma measurements from MAVEN/NGIMS and MAVEN/LPW were all included in the analysis. The top panel of Figure 5 shows the thermal pressure ( $P_{th,i}$ ) and magnetic pressure ( $P_{B,i}$ ) changes in the ionosphere near the ionopause height that were averaged within  $\pm 20$  km altitude. The magnetic pressures of the ionopause were investigated using multi-instrument measurements from MAVEN during its periapsis in the subsolar regions and Tianwen-1 during its periapsis in the antisolar regions.

The red-shaded area represents the dynamic pressure of upstream solar wind ( $P_{dyn,sw}$ ) at Mars, which is obtained from the MAVEN/LPW key parameter in the MAVEN Science Data Center using:

$$P_{dyn,sw} = \rho_{sw} u_{sw}^2 \cos^2 \chi \quad [\text{dyn cm}^{-2}] \quad (1)$$

where  $\rho_{sw}$  is the solar wind mass density,  $u_{sw}$  is the speed of solar wind, and  $\chi$  is the solar zenith angle. To select undisturbed solar wind intervals and avoid contamination from measurements taken inside the bow shock, the dynamic pressure of upstream solar wind out of the bow shock was determined from only data points with the solar wind speed  $|u_{sw}| > 200 \text{ km s}^{-1}$ , normalized magnetic-field fluctuations  $\sigma_B/|B| < 0.15$ , altitude  $R > 500 \text{ km}$ , and the ratio of proton scalar temperature to the solar wind speed  $\sqrt{T}/|u_{sw}| < 0.012$  (Halekas et al. 2017).

The yellow circles represent the thermal pressure of the nightside ionopause ( $P_{th,i}$ ) obtained by:

$$P_{th,i} = N_e k_B (T_e + T_i) \quad [\text{dyn cm}^{-2}] \quad (2)$$

where  $N_e$  is the electron density from MAVEN/LPW,  $k_B$  is the Boltzmann constant,  $T_e$  is the electron temperature from MAVEN/LPW, and  $T_i$  is the ion temperature. The ion temperature  $T_i$  is not available, and thus  $T_i$  is assumed to be approximately equal to  $T_e$  at altitudes of the ionopause above 350 km (Mendillo et al. 2011).

The blue squares and diamonds represent the magnetic pressure of the nightside and dayside ionopause ( $P_{B,i}$ ) obtained by:

$$P_{B,i} = \frac{B^2}{2\mu_0} \quad [\text{dyn cm}^{-2}] \quad (3)$$

where  $B$  is the magnetic-field magnitude from MAVEN/MAG and Tianwen-1/MOMAG, and  $\mu_0$  is the magnetic permeability of a vacuum. The horizontal components of magnetic fields were used in calculating the magnetic pressure of ionopause. The direction of the magnetic field is crucial because the vertical field in the ionosphere does not make an effective pressure perpendicular to the ionopause boundary (Sánchez-Cano et al. 2020).

The Martian ionosphere is mostly in a magnetized state (Sánchez-Cano et al. 2020). The thermal pressure of the nightside ionopause was generally less than 0.1 nPa. The thermal pressure of the ionopause is less significant compared to the magnetic pressure. The red vertical-dashed line represents the arrival time of the shock at 19:20 UT on 2021 December 8, when the dynamic pressure of solar wind was larger than 2.0 nPa. Both the magnetic pressures of the nightside and dayside ionopause were enhanced to over 0.4 nPa after the shock arrival. This indicates a transient compression at Mars, with a higher solar wind dynamic pressure driven by a fast-forward shock of the ICMEs. The gray color band between two black vertical-dashed lines represents the interval of the ICME. The magnetic pressure of the dayside ionopause returned to its previous level. The high dynamic pressure of solar wind is a very important factor that governs the response of Martian space environment to the ICME. The high solar wind dynamic pressure and foreshock pressure of this strong ICME are greater than the ionosphere pressure, allowing the solar wind to penetrate into the ionosphere and enhance the erosion of ionospheric plasma. Furthermore, the magnetic pressures on the dayside and the nightside were both simultaneously increased during the ICME passage. One reason for this is that it could be a result of the relatively close positions of MAVEN and Tianwen-1 periapses. In addition, the horizontal flow across the terminator and downward diffusion of plasma in the ionosphere could make a contribution.

It is worth noting that after the arrival of the ICME at Mars, fluctuations in the magnetic pressure of the ionopause can also be observed intermittently on the nightside but not on the dayside. The occasional disturbances in the ionospheric magnetic pressure are consistent with the previous observations that the topside Martian ionosphere becomes highly fragmented and composed of intermittent plasma with the effects of the high pressure of solar wind (Dubinin et al. 2009; Zhang et al. 2021a). The intensification of solar wind plasma and magnetic-field strength within an ICME can have a significant impact on the magnetopause and ionosphere of Mars. The size and location of the regions with open magnetic field lines can be significantly altered by the passage of a large ICME (Crider et al. 2005). The energetic electrons precipitate and ion outflow occurs due to the considerable weakness of the shielding effect of Mars' crustal fields (Lillis & Brain 2013).

The bottom panel of Figure 5 shows the column abundance density of electrons (blue),  $O_2^+$  (yellow), and  $O^+$  (red) integrated between 185–500 km, with the corresponding



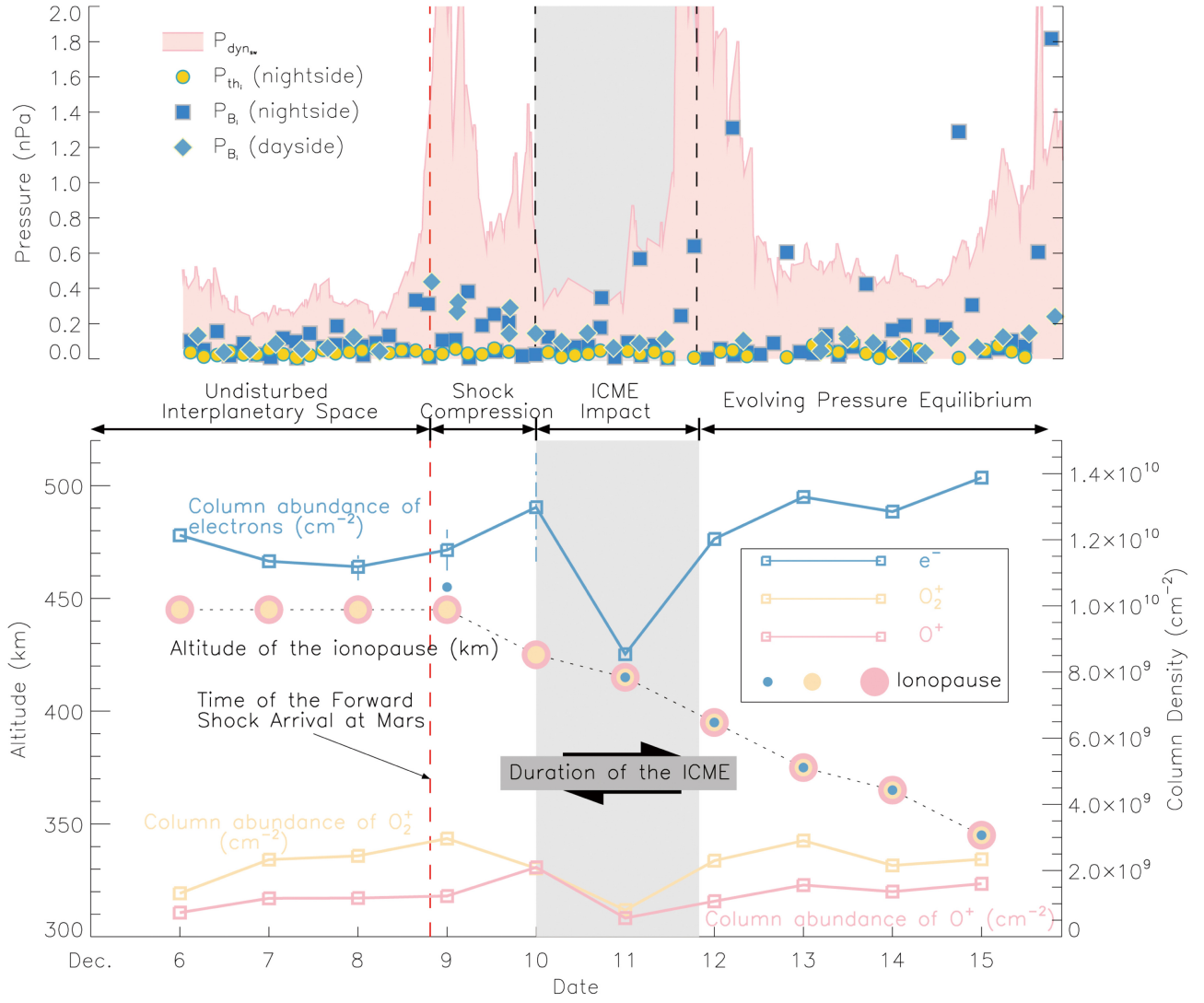


**Figure 5.** Perturbations in the Martian upper atmosphere caused by the ICME. Both the associated IMF and high-speed solar winds can remarkably influence planetary electrons and heavy ions ( $\text{O}_2^+$  and  $\text{O}^+$ ). The top panel shows the dynamic pressure of upstream solar wind out of the bow shock at Mars ( $P_{\text{dyn}_{\text{sw}}}$ ) as a red-shaded area, the thermal pressure of the nightside ionopause ( $P_{\text{thi}}$ ) as yellow circles, the magnetic pressure of the nightside ionopause ( $P_{\text{Bi}}$ ) as blue squares, and the magnetic pressure of the dayside ionopause as blue diamonds. The bottom panel shows the variations in column abundance density of electrons (blue),  $\text{O}_2^+$  (yellow), and  $\text{O}^+$  (red) for the nightside ionosphere measured by MAVEN integrated between 185–500 km, with the corresponding altitude of the ionopause as circles from density profiles for electrons,  $\text{O}_2^+$ , and  $\text{O}^+$  respectively. The blue vertical-dashed line represents the uncertainty of the column abundance density of electrons because the altitude of the ionopause cannot be precisely defined due to a data gap. The red vertical-dashed line and the gray color band are the arrival time of the ICME-driven shock and the interval of the ICME. The occurrence of reduction in the column abundance of ionospheric plasma occurred shortly after the arrival of the ICME.

altitude of the ionopause as circles from density profiles for electrons,  $\text{O}_2^+$ , and  $\text{O}^+$ , respectively. From the profiles of ion and electron densities, the height of the ionopause dramatically decreased after the arrival of the ICME shock, from 445 km altitude on December 9 to 345 km altitude on December 15. The ionopause was lowered by the high dynamic pressure of solar winds. There is an apparent depletion of the observed nightside ionosphere at the time of the ICME passage. Ions escaped to space through the interaction of the ICME and Mars. Between 00:00 on December 10 and 20:00 on December 11, the ICME passed through the space environment surrounding Mars. A significant decrease in the column abundance of ionospheric plasma was observed by MAVEN. The column abundance of electrons above 180 km decreased by 34% from  $1.3 \times 10^{10} \text{ cm}^{-2}$  on December 10 to  $8.5 \times 10^9 \text{ cm}^{-2}$  on December 11. The column abundance of  $\text{O}_2^+$  decreased by 61% from  $2.1 \times 10^9 \text{ cm}^{-2}$  on December 10 to  $8.1 \times 10^8 \text{ cm}^{-2}$

on December 11. The column abundance of  $\text{O}^+$  decreased by 73% from  $2.1 \times 10^9 \text{ cm}^{-2}$  on December 10 to  $5.7 \times 10^8 \text{ cm}^{-2}$  on December 11. Two days later, the column abundance densities of electrons,  $\text{O}_2^+$ , and  $\text{O}^+$  returned to their undisturbed levels on December 13, indicating a perpetually evolving equilibrium state. The depleted column density of electrons  $P_e$  is estimated to be  $\sim 4.5 \times 10^9 \text{ cm}^{-2}$ . Taking the width of the erosion channel  $d \sim 400 \text{ km}$  and the length of the erosion channel in the horizontal direction  $L \sim \pi/2 \cdot R$ , where  $R \sim 4000 \text{ km}$ , yields the total number of loss ions  $\sim 1.3 \times 10^{26}$ . Such an amount of ions can be lost in  $\sim 5$  minutes with a flow velocity  $V_{\text{esc}} \sim 20 \text{ km s}^{-1}$  (Dubinin et al. 2009), and thus the corresponding ion loss rate is  $4.3 \times 10^{23} \text{ s}^{-1}$ . Ion escape is minimized in the subsolar regions and enhanced in the antisolar regions (Jakosky et al. 2018). Therefore, this is a conservative estimate given that the ionospheric plasma outside of intruded regions can be driven into a global convention and

atmospheric circulation (Cui et al. 2015; Niu et al. 2020). Due to the limited coverage of observations, a direct estimation of the global loss rate of ions during ICME cannot be accurately determined. Brain et al. (2015) found that the outward flux of ions dominates the inward flux on the nightside of Mars and the outward rate of ions on the nightside is 2.5–3.0 times larger than that on the dayside. From the MAVEN measurements, Mars’s ion escape was significant during the passage of the ICME, as indicated by a noticeable drop in the averaged column density of plasma in the nighttime ionosphere.

It is interesting to note that during the passage of some ICMEs at Venus, the disappearance of the Venusian ionosphere was also observed (Cravens et al. 1982). In contrast to ionospheric holes that form in localized regions, the ionospheric plasma was depleted throughout the nightside ionosphere. The disappearing ionosphere on the nightside of Venus is attributed to the high solar wind pressure cutting off the thermal pressure gradient that drives trans terminator flow of ionosphere from the dayside. In this situation, a similar physical mechanism may apply to depletions of the observed nightside ionosphere at Mars. In addition, increasing solar wind dynamic pressure pushes the dayside ionopause lower in height. As a result, the nightside should thus be accessible to plasma at low altitudes, which is consistent with a rise in the nightside ionospheric electron density at lower altitudes in this study. Further investigations can provide insight with future multi-instrument data from Tianwen-1, MAVEN, and upcoming Mars exploration missions, which will provide supportive evidence and test the hypothesis.

#### 4. Summary

In this study, we present the day-to-day changes in the Martian upper ionosphere in response to an ICME from 2021 December 6–15 from Tianwen-1 and MAVEN observations. The ICME passed through Mars on 2021 December 10. The interplanetary space environment was quiet, and the primary interplanetary disturbances surrounding Mars were associated with the ICME. The ICME caused a fast-forward shock, a high solar wind dynamic pressure, and an intense IMF. Tianwen-1 and MAVEN observations show a great impact of the ICME on the upper atmosphere and ionosphere of Mars. The high pressure of solar winds and magnetic fields within an ICME produced substantial compression and disturbances of Mars’s space environment. The depletion of the topside Martian ionosphere on the nightside was observed as an indicator of ion escape from Mars. A sudden drop in the densities of electrons,  $O_2^+$ , and  $O^+$  in the topside ionosphere was observed from MAVEN LPW and NGIMS.

Between 2021 December 10–15, the ionopause—a sharp drop in plasma density—occurred and gradually descended from 415 to 345 km on the nightside of Mars. The column abundance of electrons,  $O_2^+$ , and  $O^+$  significantly decreased on December 11 by 34%, 61%, and 73%, respectively, compared to the ionospheric condition on December 10. The interactions between Mars’s atmosphere and solar wind are typically characterized by the formation of some plasma boundaries, e.g., the bow shock formed separating upstream solar wind and the planet inside which the solar wind is lowered (Hall et al. 2019), and the ionopause formed separating the shocked solar wind from the magnetosphere and the ionospheric plasma (Russell & Vaisberg 2008). Ion loss at Mars occurs via the acceleration of ionospheric ions in an electric field. The electric

field can be generated by many processes, including the plasma pressure gradients in the ionosphere (Collinson et al. 2015), the changes in magnetic-field configurations with compression of solar wind (Luhmann & Kozyra 1991), and plasma flow shear by the crustal magnetic anomalies (Dubinin et al. 2008).

The atmospheres of both Mars and Venus directly interact with solar wind (Dubinin et al. 2012). The disappearance of the nightside ionosphere was observed at Venus under the high pressure of solar wind as a manifestation of space weather effects (Cravens et al. 1982). The response of oxygen ion escape to the ICME was studied from Venus using Venus Express observations (Luhmann et al. 2008). Ion escape also occurs at Mars (Dubinin et al. 2009; Fan et al. 2019). Mars has relatively weak magnetic shielding from space weather due to the lack of a global intrinsic magnetic field. This means that Mars is more directly exposed to the solar wind than Earth (Wu et al. 2023). Therefore, a fast ICME arriving at Mars can cause more significant perturbations in the ionosphere, which could lead to the intensification of plasma escape. The magnetic reconnection near Mars was accompanied by the generation of plasma vortices and their escape through the tail. In the hybrid simulations, an asymmetrical void of  $O^+$  ions was seen on the nightside of Mars under conditions where solar wind velocity is  $485 \text{ km s}^{-1}$  (Dubinin et al. 2019). However, further studies of the response of the Mars to ICMEs are rather constrained due to the relatively limited observations of Mars’s space environment.

Mars provides a unique opportunity to study the weather and climate changes on a planet besides Earth. Mars atmospheric research can help us better understand how Mars evolved into its current state and what the future of Earth could be like. The in situ observations from Tianwen-1 and MAVEN at Mars and the upstream solar wind observations from BepiColombo, as well as future Mars exploration missions carried with state-of-the-art scientific instruments, will enable scientific investigations of the space environment surrounding Mars and its interaction with solar winds in response to transient solar and planetary drivers, leading to significant advances in our understanding of the history of the climate evolution of Mars and the ongoing ion loss to space.




#### Acknowledgments

We acknowledge the Tianwen-1/MOMAG team for providing the magnetic field data. The Tianwen-1/MOMAG data is accessible through the Planet Exploration Program Scientific Data Release System (<http://202.106.152.98:8081/marsdata/>) or you can download the data used in this study from the official website of the MOMAG team ([http://space.ustc.edu.cn/dreams/tw1\\_momag/](http://space.ustc.edu.cn/dreams/tw1_momag/)). All MAVEN data used in this study are available through the MAVEN Science Data Center (<https://lasp.colorado.edu/maven/sdc/public/>). The BepiColombo/MPOMAG data used in this study are available at doi:10.25392/leicester.data.22203376.v1.

This work is supported by the B-type Strategic Priority Program of CAS (grant No. XDB41000000), the National Natural Science Foundation of China (grant Nos. 42188101, 42130204), the Frontier Scientific Research Program of Deep Space Exploration Laboratory (grant No. 2022-QYKYJH-ZYTS-016) and the Joint Open Fund of Mengcheng National Geophysical Observatory (grant No. MENGO-202207). D.H. was supported by the German Ministerium für Wirtschaft und Klimaschutz and the German Zentrum für Luft- und Raumfahrt

(DLR) under contracts 50QW1501 and 50QW2202. B.S.-C is supported through the UK-STFC Ernest Rutherford Fellowship ST/V004115/1 and ST/Y000439/1.

### ORCID iDs

Bingkun Yu  <https://orcid.org/0000-0003-2758-1960>  
 Yutian Chi  <https://orcid.org/0000-0001-9315-4487>  
 Mathew Owens  <https://orcid.org/0000-0003-2061-2453>  
 Christopher J. Scott  <https://orcid.org/0000-0001-6411-5649>  
 Chenglong Shen  <https://orcid.org/0000-0002-3577-5223>  
 Luke Barnard  <https://orcid.org/0000-0001-9876-4612>  
 Ingo Richter  <https://orcid.org/0000-0002-5324-4039>  
 Jingnan Guo  <https://orcid.org/0000-0002-8707-076X>  
 Beatriz Sánchez-Cano  <https://orcid.org/0000-0003-0277-3253>  
 Zhuxuan Zou  <https://orcid.org/0009-0008-9920-9600>  
 Zhenpeng Su  <https://orcid.org/0000-0001-5577-4538>  
 Guoqiang Wang  <https://orcid.org/0000-0002-6618-4928>  
 Kai Liu  <https://orcid.org/0000-0003-2573-1531>  
 Mike Lockwood  <https://orcid.org/0000-0002-7397-2172>

### References

- Andersson, L., Ergun, R., Delory, G., et al. 2015, *SSRv*, **195**, 173  
 Barnard, L., & Owens, M. 2022, *FrP*, **10**, 1062  
 Benkhoff, J., Murakami, G., Baumjohann, W., et al. 2021, *SSRv*, **217**, 90  
 Benna, M., Mahaffy, P., Grebowsky, J., et al. 2015, *GeoRL*, **42**, 8958  
 Brain, D. A., McFadden, J., Halekas, J. S., et al. 2015, *GeoRL*, **42**, 9142  
 Carlsson, E., Fedorov, A., Barabash, S., et al. 2006, *Icar*, **182**, 320  
 Chi, Y., Scott, C., Shen, C., et al. 2021, *ApJL*, **917**, L16  
 Chi, Y., Shen, C., Cheng, L., et al. 2023a, *ApJS*, **267**, 3  
 Chi, Y., Shen, C., Liu, J., et al. 2023b, *ApJL*, **951**, L14  
 Chi, Y., Shen, C., Wang, Y., et al. 2016, *SoPh*, **291**, 2419  
 Collinson, G., Mitchell, D., Gloer, A., et al. 2015, *GeoRL*, **42**, 9128  
 Connerney, J., Espley, J., Lawton, P., et al. 2015, *SSRv*, **195**, 257  
 Cravens, T., Brace, L., Taylor, H., Jr., et al. 1982, *Icar*, **51**, 271  
 Crider, D. H., Espley, J., Brain, D., et al. 2005, *JGRA*, **110**, A09S21  
 Cui, J., Galand, M., Yelle, R., Wei, Y., & Zhang, S.-J. 2015, *JGRA*, **120**, 2333  
 Davis, C. J., Davies, J., Lockwood, M., et al. 2009, *GeoRL*, **36**, L08102  
 Dubinin, E., Chanteur, G., Fraenz, M., & Woch, J. 2008, *P&SS*, **56**, 868  
 Dubinin, E., Fraenz, M., Fedorov, A., et al. 2012, *The Plasma Environment of Venus, Mars, and Titan* (New York: Springer), 173  
 Dubinin, E., Fraenz, M., Woch, J., et al. 2009, *GeoRL*, **36**, L01105  
 Dubinin, E., Fränz, M., et al. 2006, *Icar*, **182**, 337  
 Dubinin, E., Modolo, R., Fraenz, M., et al. 2019, *GeoRL*, **46**, 12722  
 Fan, K., Fraenz, M., Wei, Y., et al. 2019, *GeoRL*, **46**, 11764  
 Fan, M., Lyu, P., Su, Y., et al. 2021, *SSRv*, **217**, 1  
 Glassmeier, K.-H., Auster, H.-U., Heyner, D., et al. 2010, *P&SS*, **58**, 287  
 Halekas, J., Ruhunusiri, S., Harada, Y., et al. 2017, *JGRA*, **122**, 547  
 Halekas, J., Taylor, E., Dalton, G., et al. 2015, *SSRv*, **195**, 125  
 Hall, B. E. S., Lester, M., Nichols, J. D., et al. 2016, *JGRA*, **121**, 4835  
 Hall, B. E. S., Sánchez-Cano, B., Wild, J. A., Lester, M., & Holmström, M. 2019, *JGRA*, **124**, 4761  
 Harada, Y., Gurnett, D., Kopf, A., et al. 2018, *GeoRL*, **45**, 7960  
 He, Z., Xu, R., Li, C., et al. 2021, *SSRv*, **217**, 9  
 Heyner, D., Auster, H.-U., Fornaçon, K.-H., et al. 2021, *SSRv*, **217**, 52  
 Jakosky, B. M., Brain, D., Chaffin, M., et al. 2018, *Icar*, **315**, 146  
 Jakosky, B. M., Grebowsky, J. M., Luhmann, J. G., et al. 2015, *Sci*, **350**, 0210  
 Kajdić, P., Sánchez-Cano, B., Neves-Ribeiro, L., et al. 2021, *JGRA*, **126**, e28442  
 Knipp, D. J., Ramsay, A., Beard, E., et al. 2016, *SpWea*, **14**, 614  
 Kong, L., Zhang, A., Tian, Z., et al. 2020, *E&PP*, **4**, 333  
 Krishnaprasad, C., Thampi, S. V., Bhardwaj, A., Pant, T. K., & Thampi, R. S. 2021, *P&SS*, **205**, 105291  
 Lee, C., Hara, T., Halekas, J., et al. 2017, *JGRA*, **122**, 2768  
 Lee, C., Jakosky, B., Luhmann, J., et al. 2018, *GeoRL*, **45**, 8871  
 Lee, C. O., Arge, C. N., Odstrčil, D., et al. 2013, *SoPh*, **285**, 349  
 Lepping, R., & Wu, C.-C. 2007, *JGRA*, **112**, A10103  
 Lester, M., Sanchez-Cano, B., Potts, D., et al. 2022, *JGRA*, **127**, e2021JA029535  
 Lillis, R. J., & Brain, D. A. 2013, *JGRA*, **118**, 3546  
 Liu, K., Hao, X., Li, Y., et al. 2020, *E&PP*, **4**, 384  
 Lockwood, M., Bentley, S. N., Owens, M. J., et al. 2019, *SpWea*, **17**, 133  
 Lockwood, M., McWilliams, K. A., Owens, M. J., et al. 2020, *JSWSC*, **10**, 30  
 Lockwood, M., Owens, M. J., Barnard, L. A., et al. 2016, *SpWea*, **14**, 406  
 Luhmann, J., Fedorov, A., Barabash, S., et al. 2008, *JGRE*, **113**, E00B04  
 Luhmann, J., & Kozyra, J. 1991, *JGR*, **96**, 5457  
 Lundin, R. 2011, *The Plasma Environment of Venus, Mars, and Titan* (New York: Springer), 309  
 Lundin, R., Barabash, S., Andersson, H., et al. 2004, *Sci*, **305**, 1933  
 Ma, Y., Fang, X., Halekas, J. S., et al. 2018, *GeoRL*, **45**, 7248  
 Mahaffy, P. R., Benna, M., King, T., et al. 2015, *SSRv*, **195**, 49  
 Mendillo, M., Lollo, A., Withers, P., et al. 2011, *JGRA*, **116**, A11  
 Meng, Q., Wang, D., Wang, X., et al. 2021, *SSRv*, **217**, 1  
 Mishra, W., Dave, K., Srivastava, N., & Teriaca, L. 2021, *MNRAS*, **506**, 1186  
 Nagy, A. F., & Schunk, R. W. 2009, *Ionospheres: Physics, Plasma Physics, and Chemistry* (Cambridge: Cambridge Univ. Press)  
 Niu, D.-D., Cui, J., Gu, H., et al. 2020, *JGRA*, **125**, e27670  
 Owens, M., Lang, M., Barnard, L., et al. 2020, *SoPh*, **295**, 1  
 Owens, M. J., Lockwood, M., Barnard, L. A., et al. 2021, *SoPh*, **296**, 82  
 Richardson, I. G., & Cane, H. V. 2012, *JSWSC*, **2**, A01  
 Russell, C., & Vaisberg, O. 2008, in *The Interaction of the Solar Wind with Venus*, ed. D. M. Hunten et al. (Tucson, AZ: Univ. Arizona Press)  
 Sánchez-Cano, B., Blelly, P.-L., Lester, M., et al. 2019, *JGRA*, **124**, 4556  
 Sánchez-Cano, B., Hall, B., Lester, M., et al. 2017, *JGRA*, **122**, 6611  
 Sánchez-Cano, B., Narvaez, C., Lester, M., et al. 2020, *JGRA*, **125**, e28145  
 Shen, C., Chi, Y., Wang, Y., Xu, M., & Wang, S. 2017, *JGRA*, **122**, 5931  
 Tang, S., Wang, Y., Zhao, H., et al. 2020, *E&PP*, **4**, 355  
 Vogt, M. F., Withers, P., Mahaffy, P. R., et al. 2015, *GeoRL*, **42**, 8885  
 Wan, W., Wang, C., Li, C., & Wei, Y. 2020, *NatAs*, **4**, 721  
 Wang, C., Xu, M., Shen, C., Chi, Y., & Wang, Y. 2021a, *ApJ*, **912**, 85  
 Wang, N., Yue, J., Wang, W., et al. 2021b, *JGRA*, **126**, e29029  
 Wang, Y., Zhang, T., Wang, G., et al. 2023, *E&PP*, **7**, 1  
 Wu, C.-C., Gopalswamy, N., Lepping, R. P., & Yashiro, S. 2013, *Terr. Atmos. Ocean. Sci.*, **24**, 233  
 Wu, S., Wu, X., Cui, J., et al. 2023, *ApJ*, **943**, 154  
 Xu, M., Shen, C., Wang, C., et al. 2022, *ApJL*, **930**, L11  
 Xu, S., Fang, X., Mitchell, D. L., et al. 2018, *GeoRL*, **45**, 7337  
 Xue, X., Wang, Y., Ye, P., Wang, S., & Xiong, M. 2005, *P&SS*, **53**, 443  
 Yashiro, S., Gopalswamy, N., Michalek, G., et al. 2004, *JGRA*, **109**, A07105  
 Younas, W., Amory-Mazaudier, C., Khan, M., & Fleury, R. 2020, *JGRA*, **125**, e27981  
 Yu, B., Scott, C. J., Xue, X., et al. 2021, *ApJ*, **916**, 106  
 Yu, G., Liu, E., Liu, G., et al. 2020, *E&PP*, **4**, 364  
 Zhang, C., Rong, Z., Nilsson, H., et al. 2021a, *ApJL*, **922**, L33  
 Zhang, J., Richardson, I., Webb, D., et al. 2007, *JGRA*, **112**, A10102  
 Zhang, J., Temmer, M., Gopalswamy, N., et al. 2021b, *PEPS*, **8**, 56  
 Zou, Y., Zhu, Y., Bai, Y., et al. 2021, *AdSpR*, **67**, 812  
 Zou, Z., Wang, Y., Zhang, T., et al. 2023, *Sci. China Technol. Sci.*, in press